Article

Fractional quantum anomalous Hall effect in multilayer graphene

https://doi.org/10.1038/s41586-023-07010-7

Received: 1 October 2023

Accepted: 21 December 2023

Published online: 21 February 2024

Check for updates

Zhengguang Lu[1,4], Tonghang Han[1,4], Yuxuan Yao[1,4], Aidan P. Reddy[1], Jixiang Yang[1], Junseok Seo[1], Kenji Watanabe[2], Takashi Taniguchi[3], Liang Fu[1] & Long Ju[1]✉

The fractional quantum anomalous Hall effect (FQAHE), the analogue of the fractional quantum Hall effect[1] at zero magnetic field, is predicted to exist in topological flat bands under spontaneous time-reversal-symmetry breaking[2–6]. The demonstration of FQAHE could lead to non-Abelian anyons that form the basis of topological quantum computation[7–9]. So far, FQAHE has been observed only in twisted $MoTe_2$ at a moiré filling factor $\upsilon > 1/2$ (refs. 10–13). Graphene-based moiré superlattices are believed to host FQAHE with the potential advantage of superior material quality and higher electron mobility. Here we report the observation of integer and fractional QAH effects in a rhombohedral pentalayer graphene–hBN moiré superlattice. At zero magnetic field, we observed plateaus of quantized Hall resistance $R_{xy} = \frac{h}{\upsilon e^2}$ at $\upsilon = 1, 2/3, 3/5, 4/7, 4/9, 3/7$ and $2/5$ of the moiré superlattice, respectively, accompanied by clear dips in the longitudinal resistance R_{xx}. R_{xy} equals $\frac{2h}{e^2}$ at $\upsilon = 1/2$ and varies linearly with υ, similar to the composite Fermi liquid in the half-filled lowest Landau level at high magnetic fields[14–16]. By tuning the gate-displacement field D and υ, we observed phase transitions from composite Fermi liquid and FQAH states to other correlated electron states. Our system provides an ideal platform for exploring charge fractionalization and (non-Abelian) anyonic braiding at zero magnetic field[7–9,17–19], especially considering a lateral junction between FQAHE and superconducting regions in the same device[20–22].

The fractional quantum Hall effect observed in conventional two-dimensional electron gas (2DEGs) at the semiconductor interface is a classic example of intertwined electron correlation and topology effects in condensed matter physics[1]. It has been proposed that similar exotic states could exist at zero magnetic field, by engineering flat electronic bands with non-zero Chern numbers[2–6]. As a precursor of the fractional quantum anomalous Hall effect (FQAHE), the integer quantum anomalous Hall effect (IQAHE) has been conceived[23] and realized in magnetic topologic insulators and moiré superlattices made of two-dimensional materials[24–27]. Recently, FQAHE has been proposed in twisted transition metal dichalcogenide (TMD) moiré superlattices[28–32] and observed in twisted $MoTe_2$ (t-$MoTe_2$) at filling factors $\upsilon > 1/2$ (refs. 10–13). Graphene-based moiré superlattices have also been proposed to host FQAH states[33–38], and could potentially show a plethora of fractional states due to fewer defects in the graphene lattice than in TMD lattices. Although fractional Chern insulators have been observed in graphene-based moiré superlattices at high magnetic fields[39,40], observation of FQAHE in any graphene system has not been reported so far.

The moiré superlattice formed between rhombohedral graphene and hexagonal boron nitride (hBN) has been demonstrated to be a remarkable platform for emergent quantum phenomena. In the highly tuneable electronic bands in crystalline multilayer rhombohedral graphene, correlated insulators, superconductivity, Chern insulators, orbital magnetism and multiferroicity have been demonstrated (Methods). When placed on hBN to form a moiré superlattice, rhombohedral graphene shows Mott insulators, tuneable ferromagnetism and Chern insulators, as well as superconductivity (Methods). On the basis of a tight-binding calculation, the band dispersion at zero gate-displacement field D becomes flatter as the layer number increases from $n = 2$ to 5, whereas the valence band starts to suffer from increased trigonal warping with $n > 5$ (ref. 41). At non-zero Ds, states near the band edge acquire larger Berry curvatures[41,42] that enable the formation of a topological flat band when a moiré potential from hBN is introduced[36,43]. Therefore, engineering topological flat bands in gate-tuned multilayer rhombohedral graphene–hBN is a promising approach for realizing FQAHE. From an experimental point of view, the rhombohedral graphene–hBN moiré superlattice features three advantages over twisted TMD moiré superlattices: (1) the higher material quality of graphene over TMD; (2) better electrical contact to graphene than to TMD and (3) the twist angle inhomogeneity induces fewer variations of the moiré period in a hetero-bilayer moiré than in a homo-bilayer moiré. Whereas the Chern insulator state has been observed in trilayer rhombohedral graphene–hBN at integer moiré fillings (Methods), FQAHE has not been found in this system so far.

[1]Department of Physics, Massachusetts Institute of Technology, Cambridge, MA, USA. [2]Research Center for Electronic and Optical Materials, National Institute for Materials Science, Tsukuba, Japan. [3]Research Center for Materials Nanoarchitectonics, National Institute for Materials Science, Tsukuba, Japan. [4]These authors contributed equally: Zhengguang Lu, Tonghang Han, Yuxuan Yao. ✉e-mail: longju@mit.edu

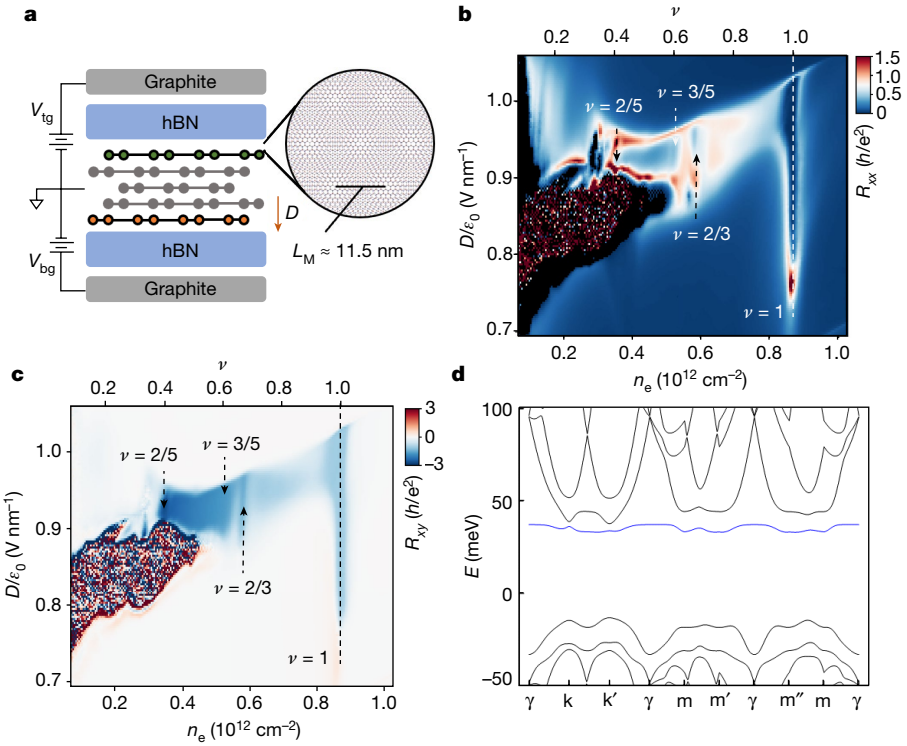

Fig. 1 | Device configuration, topological flat band and phase diagram of the rhombohedral pentalayer graphene–hBN moiré superlattice. **a**, Schematic of the device configuration, showing a moiré superlattice between the top layer of graphene and the top hBN, with a moiré period of 11.5 nm. **b**,**c**, Phase diagrams of the device revealed by symmetrized R_{xx} (**b**) and antisymmetrized R_{xy} (**c**) at $B = \pm 0.1$ T as functions of n_e (υ) and D. The temperature at the mixing chamber of dilution refrigerator is 10 mK. Large anomalous Hall signals emerge in a tilted stripe region centred at $D/\varepsilon_0 \cong 0.93$ V nm^{-1}. Clear dips of R_{xx} can be seen at filling factors of the moiré superlattice $\upsilon = 1, 2/3, 3/5$ and $2/5$ (indicated by the dashed lines and arrows), where R_{xy} shows plateaus of values. **d**, Calculated band structure of our moiré superlattice with interlayer potential $\Delta = 75$ meV, showing a flat $|C| = 1$ moiré conduction band and a dispersive $C = 0$ moiré valence band.

Here we report observations of IQAHE and FQAHEs in a new graphene moiré system formed by pentalayer rhombohedral graphene and hBN, as shown in Fig. 1a. Although the general possibility of FQAHE in rhombohedral graphene–hBN moiré superlattices has been suggested before[36], the pentalayer system we study has not received any concrete theoretical analysis or predictions. The superlattice period is roughly 11.5 nm and the twist angle is roughly 0.77°. We observed quantized Hall resistance $R_{xy} = \pm \frac{h}{e^2}$ at a moiré superlattice filling factor $\upsilon = 1$ and zero magnetic field. These states correspond to Chern numbers $C = \pm 1$. At fractional filling factors between 0 and 1, we observed six states with fractionally quantized Hall resistances $R_{xy} = \frac{h}{ve^2}$ at zero magnetic field. We observed $R_{xy} = \frac{2h}{e^2}$ at $\upsilon = 1/2$ and a linear dependence of R_{xy} on υ. By tuning D, we observed phase transitions from composite Fermi liquid (CFL) to valley-polarized Fermi liquid and a correlated insulator. We have measured two devices with similar moiré superlattice periods and they both show IQAHE and FQAHE. The data presented in the main text are based on device 1, and the data from device 2 are included in Extended Data Figs. 8 and 9.

Phase diagram of the Moiré superlattice

Figure 1b,c shows the longitudinal resistance R_{xx} and transverse resistance R_{xy} as functions of charge density n_e (filling factor υ) and D measured at mixing chamber temperature $T = 10$ mK. R_{xx} and R_{xy} have been symmetrized and antisymmetrized using data collected at $B = \pm 0.1$ T (Methods and Extended Data Fig. 4). Whereas most regions on the maps show small R_{xx} and R_{xy}, large values of resistances emerge in a tilted stripe region. At small υ up to 1/2, a large R_{xx} emerges, whereas R_{xy} shows large fluctuations around zero. At $\upsilon = 2/5$ to 1, a large R_{xy} emerges and gradually changes with υ. At $\upsilon = 1, 2/3, 3/5$ and $2/5$, R_{xx} shows local minimums whereas R_{xy} shows plateaus as a function of υ. As we show in the following sections, these states feature quantized R_{xy} as expected for IQAHE and FQAHEs. We note that the charge density corresponding to $\upsilon = 1$ in our system is about five times smaller than that in t-$MoTe_2$ (refs. 10–13) due to the larger moiré superlattice period.

The insulating state with large R_{xx} we observed at $\upsilon \leq 1/2$ occupies a large continuous range of filling factor, which is distinct from correlated insulators at integer filling factors or generalized Wigner crystals at discrete fractional filling factors of moiré superlattices[44,45]. It is possible, for example, that electron crystallization happens within the flat moiré conduction band and leads to a Wigner crystal state at zero magnetic field[46]. At $D < 0$, we observed correlated insulating states at integer filling factors $\upsilon = 2, 3$ and 4 (Extended Data Fig. 1). The existence of topological states and correlated insulating states at opposite Ds are consistent with previous experiments on rhombohedral graphene–hBN moiré superlattices (Methods). In this work, we focus on the regime of large positive displacement fields.

In the tilted stripe region, the large anomalous Hall signals indicates spontaneous valley polarization that breaks the time-reversal symmetry. As the D required to observe the anomalous Hall signal is high, at finite charge density, the redistribution of charges is expected to partially screen the externally applied D. This picture may explain the slope of the striped region, in which a larger D is needed to maintain a narrow bandwidth as υ increases. The observation of IQAHE and FQAHEs at $\upsilon \leq 1$ further suggests the presence of a topological flat band.

Figure 1d shows a moiré band structure calculated from a tight-binding model for pentalayer rhombohedral graphene[43], with an added phenomenological superlattice potential to account for moiré effects from the nearly aligned hBN layer. For a top-to-bottom interlayer potential difference $\Delta = 75$ meV, this model produces a $|C| = 1$ lowest

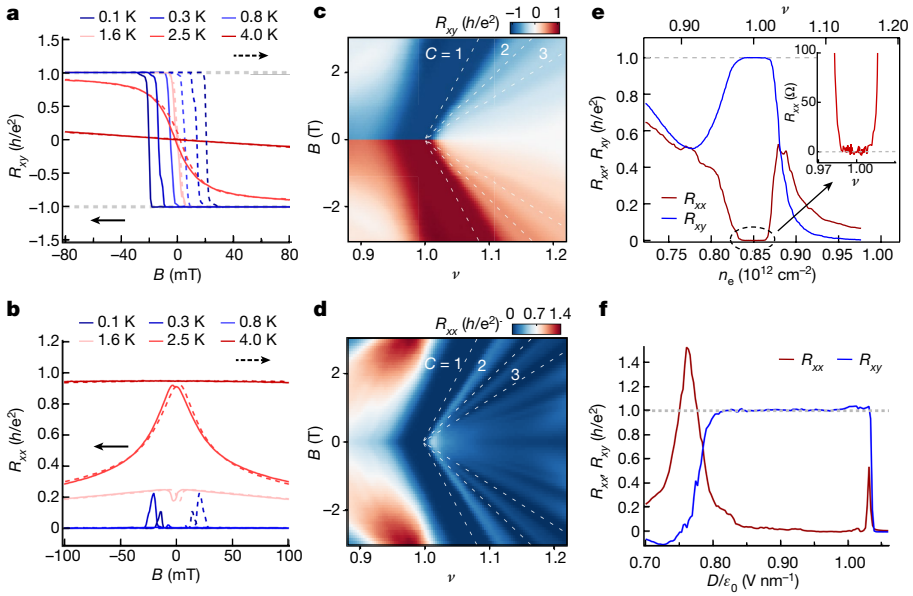

Fig. 2 | IQAHE. a,**b**, Magnetic hysteresis scans of R_{xy} (**a**) and R_{xx} (**b**) at $\upsilon = 1$ and $D/\varepsilon_0 = 0.97$ V nm^{-1} and $T = 0.1$–4 K. Solid (dashed) lines correspond to scanning B from positive (negative) values to negative (positive) values. At 0.1 K, R_{xy} is quantized at $\pm\frac{h}{e^2}$ that corresponds to a Chern number $C = \pm 1$, whereas R_{xx} shows a value less than 5 Ω at $B = 0$ mT. **c**,**d**, Landau fan diagrams of R_{xy} (**c**) and R_{xx} (**d**) at $D/\varepsilon_0 = 0.97$ V nm^{-1}. The IQAH state can be seen as a wide plateau in both maps, which disperses with magnetic field with a slope that agrees well with the dashed lines (corresponding to $C = \pm 1$, as determined by Streda's formula). At above roughly 0.6 T, features associated with integer quantum Hall states start to appear, corresponding to $C = \pm 2$ and 3, as indicated by extra dashed lines. **e**, Symmetrized R_{xx} and antisymmetrized R_{xy} (we present the positive values for convenience) as functions of υ at $T = 10$ mK and $D/\varepsilon_0 = 0.97$ V nm^{-1}, featuring quantized R_{xy} in a plateau with a width of roughly 3×10^{10} cm^{-2}. The inset shows a zoomed-in plot to reveal the plateau of $R_{xx} < 5$ Ω. **f**, R_{xx} and R_{xy} as a function of D at $\upsilon = 1$, featuring a wide plateau at roughly 0.8–1.03 V nm^{-1}. Moving to both higher and lower Ds, the device transitions to metallic states with small R_{xx} and R_{xy}. A peak in R_{xx} appears during both transitions.

conduction moiré band that is extremely narrow (bandwidth less than 5 meV) and isolated from other bands with a global band gap. By contrast, the lowest valence moiré band is notably broader (bandwidth greater than 45 meV), topologically trivial ($C = 0$) and energetically overlaps with adjacent moiré bands.

IQAHE

Figure 2 shows detailed characterizations of the anomalous Hall state at $\upsilon = 1$. At $D/\varepsilon_0 = 0.97$ V nm^{-1}, both R_{xy} and R_{xx} show hysteretic behaviours under scanned magnetic field, as shown in Fig. 2a,b. At $T = 0.1$ K, R_{xy} is quantized at $\frac{h}{e^2}$ at zero magnetic field, whereas R_{xx} is smaller than 5 Ω. R_{xy} remains quantized up to at least 1.6 K and R_{xx} remains small in the same temperature range. Figure 2c,d shows the B-dependence of R_{xy} and R_{xx} in the vicinity of $\upsilon = 1$ at $D/\varepsilon_0 = 0.97$ V nm^{-1}. The anomalous Hall state persists to $B = 0$ T and shows a wide plateau in both R_{xy} and R_{xx}. The dispersion of this state agrees well with a Chern number $C = \pm 1$ state (indicated by the dashed line) according to Streda's formula. Starting from roughly 0.6 T, more dips in R_{xx} emerge and their slopes with B agree with $C = 2$ and 3 states (indicated by extra dashed lines). Figure 2e shows the n_e (υ) dependence of R_{xy} and R_{xx} and features a plateau with a width of $\Delta n_e \cong 3 \times 10^{10}$ cm^{-2}. The quantized R_{xy} and small R_{xx} values of the state at $\upsilon = 1$ exist in a wide range of D, as shown in Fig. 2f. At both higher and lower Ds, the device shows small R_{xx} and R_{xy}, except for a peak of R_{xx} during both transitions.

These observations indicate the IQAHE with $C = \pm 1$ at filling factor $\upsilon = 1$. The features corresponding to $C = 2$ and 3 are due to integer quantum Hall effects that emerge at a low magnetic field, which demonstrates the high electron mobility of our device. The incremental change $\Delta C = 1$ between these three features indicates that the isospin degeneracy is completely lifted at $\upsilon = 1$, which corresponds to one electron per moiré unit cell. The width of the IQAHE plateau corresponds to a roughly ten times smaller charge density than that in t-$MoTe_2$ (refs. 11,13).

FQAHE

As shown by Fig. 1b,c, large anomalous Hall response is found in a wide range between $\upsilon = 2/5$ and 1. Figure 3a,b shows finer maps of R_{xx} and R_{xy} in this range in which extra vertical line features can be seen. To better visualize the states corresponding to these lines, in Fig. 3c we show line cuts along the dashed lines in Fig. 3a,b. We can observe plateaus of R_{xy} at $\upsilon = 2/5$, 3/7, 4/9, 4/7, 3/5 and 2/3 with the value of R_{xy} quantized at $\frac{h}{\nu e^2}$. At the same time, R_{xx} shows clear dips at these filling factors, similar to the observations of fractional quantum Hall states in 2DEGs at high magnetic fields[1,14]. We note that the $\upsilon = 2/5$ state is right next to the boundary of the anomalous Hall region, which shows a peak in R_{xx}. Nevertheless, the clear plateau of R_{xy} and dip in R_{xx} are observed at $\upsilon = 2/5$. Figure 3d–f,h–j shows the magnetic hysteresis scans at fractional filling factors corresponding to the states identified in Fig. 3c. For all these states, R_{xy} shows quantized values of $\frac{h}{\nu e^2}$ whereas R_{xx} is much smaller than R_{xy}. Last, Fig. 3g,k shows the Landau fan diagram of R_{xx} in the range of $\upsilon < 1/2$ and $\upsilon > 1/2$, respectively. The dips at fractional filling factors evolve into tilted lines whose slopes agree well with the dashed lines, which are calculated on the basis of Streda's formula $\frac{\partial n_e}{\partial B} = \frac{\nu e}{h}$ for the corresponding filling factors. As a function of D, all FQAH states develops a plateau of R_{xy} at the corresponding quantized values (Extended Data Fig. 2) and dips of R_{xx}. The centre of the R_{xy} plateau and the dips in R_{xx} shift to higher D as the filling factor increases, which agrees with the tilted stripe shape of the anomalous Hall region as shown in Fig. 1b,c.

The observations of quantized R_{xy} and the corresponding dips in R_{xx} at fractional filling factors, together with the hysteresis enclosing a zero magnetic field indicate FQAH states in our graphene-based moiré superlattice. These states resemble the Jain sequence of fractional quantum Hall states[14–16], but at zero magnetic field. Compared with t-$MoTe_2$ in which FQAHEs are only observed at $\upsilon > 1/2$ (refs. 10–13), the fractional states we observed reside at both sides

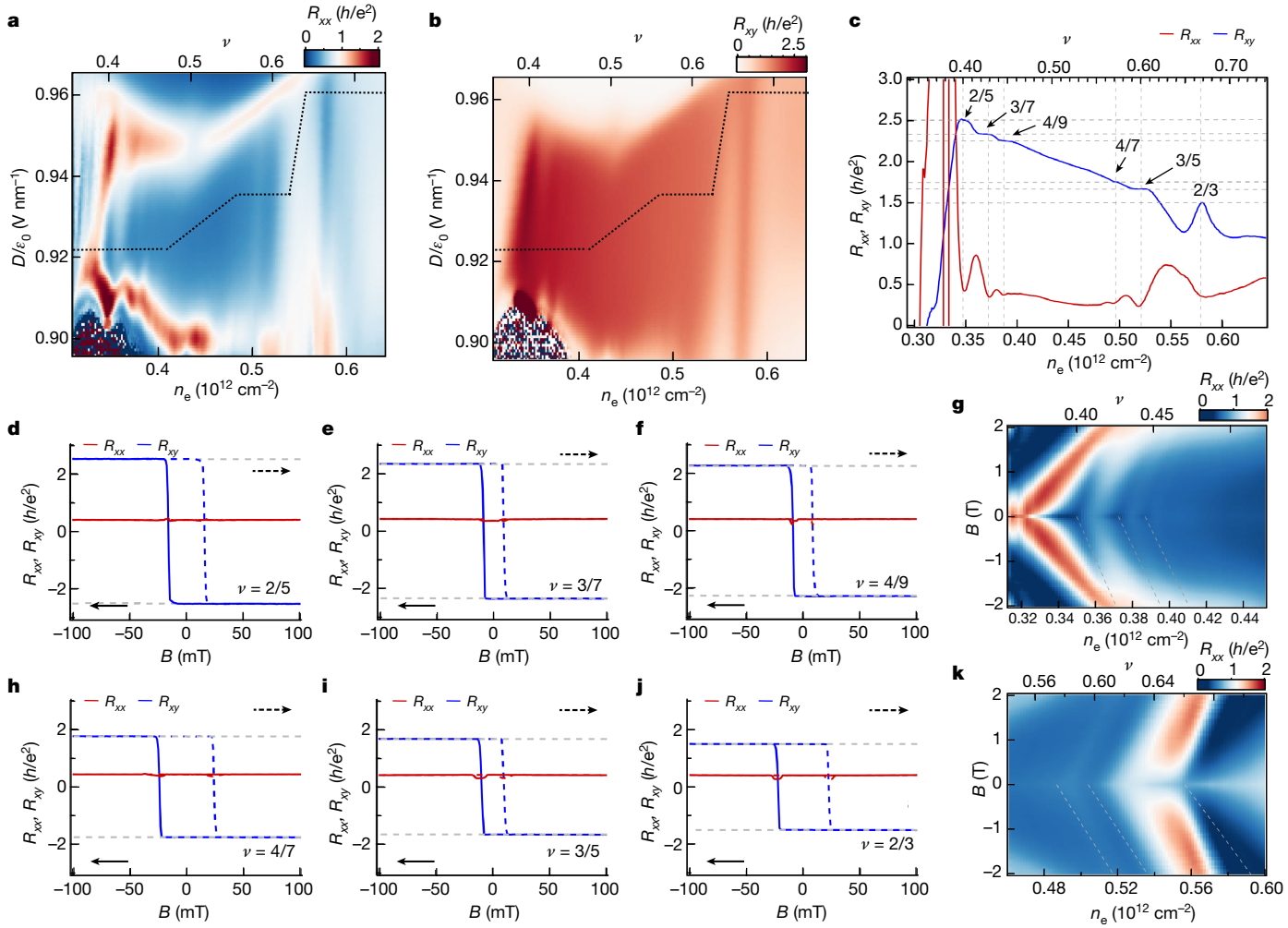

Fig. 3 | FQAHEs. a,**b**, Zoomed-in diagrams of symmetrized R_{xx} (**a**) and antisymmetrized R_{xy} (**b**) (we present the positive values for convenience) at $B = \pm 0.1$ T as functions of ν (n_e) and D. Fine features that could not be identified in Fig. 1d,e can be seen in the vicinity of $\nu = 1/2$, especially in the R_{xx} diagram. Data are collected using a constant voltage bias measurement. **c**, R_{xx} and R_{xy} along the dashed lines in **a** and **b**, taken with a constant current measurement. Clear plateaus of R_{xy} at $\frac{5h}{2e^2}$, $\frac{7h}{3e^2}$, $\frac{9h}{4e^2}$, $\frac{7h}{4e^2}$, $\frac{5h}{3e^2}$ and $\frac{3h}{2e^2}$ emerge at $\nu = 2/5$, 3/7, 4/9, 4/7, 3/5 and 2/3, as indicated by the dashed lines and arrows. R_{xx} shows clear dips at the corresponding filling factors. **d**–**f**,**h**–**j**, Magnetic hysteresis scans of R_{xy} and R_{xx} at $\nu = 2/5$ (**d**), 3/7 (**e**), 4/9 (**f**), 4/7 (**h**), 3/5 (**i**) and 2/3 (**j**), showing quantized values of $R_{xy} = \frac{h}{\nu e^2}$ and much smaller R_{xx}. **g**,**k**, Landau fan diagrams of R_{xx} at $D/\varepsilon_0 = 0.92$ V nm^{-1}. The FQAH states can be seen as tilted line features, the slopes of which agree well with the dashed lines. The slopes of dashed lines correspond to $C = 2/5$, 3/7 and 4/9 (**g**), and 4/7, 3/5 and 2/3 (**k**) using Streda's formula.

of the half-filling. This is probably due to the better electrical contact in graphene devices than that which has been achieved in semiconductor devices at low charge densities. The narrowest plateau width of FQAH states we have observed is roughly 10^{10} cm^{-2}, which is about ten times narrower than the 3/5 state observed in t-$MoTe_2$ (ref. 11).

AHE and phase transitions at $\nu = 1/2$

In addition to FQAHE states that have plateaus in R_{xy} and dips in R_{xx}, we observed a continuously changing anomalous Hall resistance in a wide range of filling factors from 4/9 to 4/7. Especially at around $\nu = 1/2$, R_{xy} varies roughly linearly with n_e and ν whereas R_{xx} does not show any clear dips, as shown in Fig. 4a. At $\nu = 1/2$, R_{xy} equals $\frac{2h}{e^2}$. Figure 4b shows the hysteretic behaviours of R_{xy} and R_{xx} under a sweeping magnetic field. Figure 4c shows the D dependence of R_{xy} and R_{xx} at a fixed filling factor $\nu = 1/2$. The value of R_{xy} spans in a plateau that is concurrent with small values of R_{xx}. At higher D, R_{xy} decreases monotonically whereas R_{xx} first increases and then decreases. At lower D, R_{xx} shoots up and R_{xy} shows large fluctuations in the range of 0.85 to 0.9 V nm^{-1}. At even lower D, R_{xy} becomes almost zero whereas R_{xx} remains at a few kΩ. At higher D than that of the $R_{xy} = \frac{2h}{e^2}$ plateau, R_{xy} decreases monotonically whereas R_{xx} first increases and then decreases. As shown in Fig. 4d, the state at $D/\varepsilon_0 = 0.97$ V nm^{-1} features small values of R_{xy} and R_{xx}, but a decent value of the Hall angle $\theta_H \cong 9.5°$ corresponding to $\tan\theta_H = \frac{R_{xy}}{R_{xx}} \cong 0.17$.

The absence of a dip in R_{xx} at $\nu = 1/2$ and the linear dependence of R_{xy} with ν in the neighbourhood are distinct from FQAH states we described in the previous section and suggest the absence of a charge gap[11,47,48]. These latter properties are reminiscent of the CFL in the half-filled lowest Landau level of 2DEGs at high magnetic fields[14–16]. Starting from the zero magnetic field CFL state, our data indicate two distinct types of phase transition driven by D. At the higher D side of the CFL state, the system is in a valley-polarized metallic state due to the non-zero anomalous Hall resistance and small R_{xx}. The persistence of valley polarization and the peak of R_{xx} at intermediate Ds suggest that it is a continuous phase transition from CFL to Fermi liquid. This new type of phase transition has been recently proposed by theory in FQAHE systems but was not observed in t-$MoTe_2$ (refs. 49,50). At the lower D

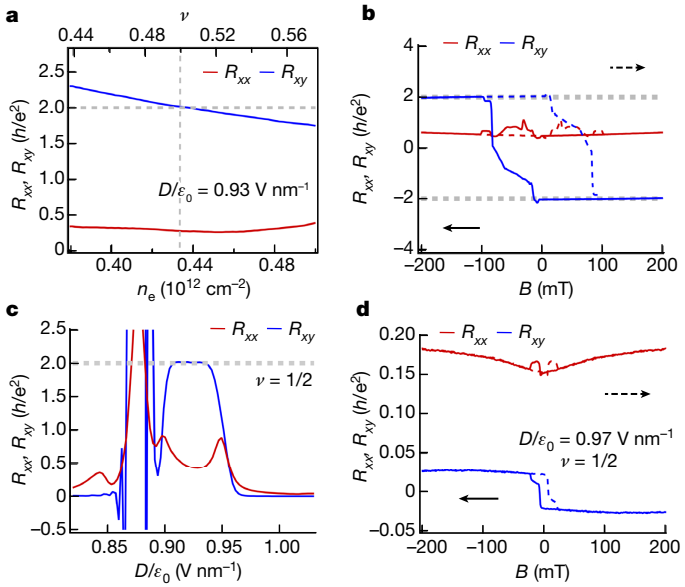

Fig. 4 | Anomalous Hall effect and phase transitions at half-filling. **a**, Symmetrized R_{xx} and antisymmetrized R_{xy} (we present the positive values for convenience) at $B = \pm 0.1$ T and $D/\varepsilon_0 = 0.93$ V nm^{-1} in the neighbourhood of half-filling. R_{xy} shows a value of $\frac{2h}{e^2}$ at $\nu = 1/2$ and varies roughly linearly with the change of filling factor, whereas no dip in R_{xx} is observed. These observations resemble the signatures of CFL in 2DEGs at high magnetic fields. **b**, Magnetic hysteresis scans of R_{xy} and R_{xx} at $\nu = 1/2$, showing R_{xy} plateaus at $\pm\frac{2h}{e^2}$ and much smaller R_{xx}. **c**, R_{xy} and R_{xx} at $\nu = 1/2$ as functions of D, showing the same R_{xy} value in a plateau spanning from 0.9 to 0.94 V nm^{-1}. At higher D, both R_{xy} and R_{xx} decrease to close to zero. At lower D, R_{xx} shoots up whereas R_{xy} shows large fluctuations at around zero. **d**, Magnetic hysteresis scans of R_{xy} and R_{xx} at $\nu = 1/2$ and $D/\varepsilon_0 = 0.97$ V nm^{-1}, showing anomalous Hall signals and a Hall angle $\theta_H \cong 9.5°$, corresponding to $\tan\theta_H = \frac{R_{xy}}{R_{xx}} \approx 0.17$. This indicates a phase transition from CFL to valley-polarized metal at the higher D side. At the lower D side, the phase transition happens between CFL and a correlated insulating state.

side, we have a phase transition from CFL to our observed correlated insulator at $\nu \leq 1/2$. Our observations call for further experiments to explore both types of phase transition, which are beyond the scope of this work.

Conclusion and outlook

We observed IQAHE at $\nu = 1$ and FQAHEs at both sides of half-filling of the first moiré conduction band. Beyond the specific moiré superlattice demonstrated here, our results indicate the great potential of similar rhombohedral graphene–hBN systems with varied layer number, gate-displacement field and twist angle for FQAHE studies: an opportunity that has been largely overlooked by theory and experiment so far. Given the high material quality, further opportunities to research new quantum phase transitions, electron crystals at zero magnetic field and behaviours of CFL in the moiré potential are within the reach of experiments[47,48]. The possibility of high-Chern-number flat bands in rhombohedral graphene (Methods) also points to possibly more exotic FQAH states with non-Abelian anyons for topological quantum computation[7–9]. Furthermore, the co-existence of FQAHE and superconductivity (Methods) in graphene systems facilitates the realization of synthetic non-Abelian anyonic braiding by using a lateral junction within the same device[20–22].

Online content

Any methods, additional references, Nature Portfolio reporting summaries, source data, extended data, supplementary information, acknowledgements, peer review information; details of author contributions and competing interests; and statements of data and code availability are available at https://doi.org/10.1038/s41586-023-07010-7.

1. Tsui, D. C., Stormer, H. L. & Gossard, A. C. Two-dimensional magnetotransport in the extreme quantum limit. *Phys. Rev. Lett.* **48**, 1559–1562 (1982).
2. Neupert, T., Santos, L., Chamon, C. & Mudry, C. Fractional quantum Hall states at zero magnetic field. *Phys. Rev. Lett.* **106**, 236804 (2011).
3. Tang, E., Mei, J. W. & Wen, X. G. High-temperature fractional quantum Hall states. *Phys. Rev. Lett.* **106**, 236802 (2011).
4. Regnault, N. & Bernevig, B. A. Fractional Chern insulator. *Phys. Rev. X* **1**, 021014 (2011).
5. Sheng, D. N., Gu, Z. C., Sun, K. & Sheng, L. Fractional quantum Hall effect in the absence of Landau levels. *Nat. Commun.* **2**, 389 (2011).
6. Sun, K., Gu, Z., Katsura, H. & Das Sarma, S. Nearly flatbands with nontrivial topology. *Phys. Rev. Lett.* **106**, 236803 (2011).
7. Moore, G. & Read, N. Nonabelions in the fractional quantum hall effect. *Nucl. Phys. B* **360**, 362–396 (1991).
8. Wen, X. G. Non-Abelian statistics in the fractional quantum Hall states. *Phys. Rev. Lett.* **66**, 802 (1991).
9. Nayak, C., Simon, S. H., Stern, A., Freedman, M. & Das Sarma, S. Non-Abelian anyons and topological quantum computation. *Rev. Mod. Phys.* **80**, 1083–1159 (2008).
10. Cai, J. et al. Signatures of fractional quantum anomalous Hall states in twisted $MoTe_2$. *Nature* https://doi.org/10.1038/s41586-023-06289-w (2023).
11. Park, H. et al. Observation of fractionally quantized anomalous Hall effect. *Nature* https://doi.org/10.1038/S41586-023-06536-0 (2023).
12. Zeng, Y. et al. Thermodynamic evidence of fractional Chern insulator in moiré $MoTe_2$. *Nature* https://doi.org/10.1038/S41586-023-06452-3 (2023).
13. Xu, F. et al. Observation of integer and fractional quantum anomalous Hall effects in twisted bilayer $MoTe_2$. *Phys. Rev. X* **13**, 031037 (2023).
14. Willett, R. et al. Observation of an even-denominator quantum number in the fractional quantum Hall effect. *Phys. Rev. Lett.* **59**, 1776 (1987).
15. Jain, J. K. Composite-fermion approach for the fractional quantum Hall effect. *Phys. Rev. Lett.* **63**, 199 (1989).
16. Halperin, B. I., Lee, P. A. & Read, N. Theory of the half-filled Landau level. *Phys. Rev. B* **47**, 7312 (1993).
17. Nakamura, J., Liang, S., Gardner, G. C. & Manfra, M. J. Direct observation of anyonic braiding statistics. *Nat. Phys.* **16**, 931–936 (2020).
18. Bartolomei, H. et al. Fractional statistics in anyon collisions. *Science* **368**, 173–177 (2020).
19. Kundu, H. K., Biswas, S., Ofek, N., Umansky, V. & Heiblum, M. Anyonic interference and braiding phase in a Mach-Zehnder interferometer. *Nat. Phys.* **19**, 515–521 (2023).
20. Lindner, N. H., Berg, E., Refael, G. & Stern, A. Fractionalizing Majorana fermions: non-Abelian statistics on the edges of abelian quantum Hall states. *Phys. Rev. X* **2**, 041002 (2012).
21. Clarke, D. J., Alicea, J. & Shtengel, K. Exotic non-Abelian anyons from conventional fractional quantum Hall states. *Nat. Commun.* **4**, 1348 (2013).
22. Vaezi, A. Fractional topological superconductor with fractionalized Majorana fermions. *Phys. Rev. B Condens. Matter Mater. Phys.* **87**, 035132 (2013).
23. Haldane, F. D. M. Model for a quantum Hall effect without Landau levels: condensed-matter realization of the 'parity anomaly'. *Phys. Rev. Lett.* **61**, 2015–2018 (1988).
24. Chang, C. Z. et al. Experimental observation of the quantum anomalous Hall effect in a magnetic topological insulator. *Science* **340**, 167–170 (2013).
25. Deng, Y. et al. Quantum anomalous Hall effect in intrinsic magnetic topological insulator. *Science* **367**, 895–900 (2020).
26. Serlin, M. et al. Intrinsic quantized anomalous Hall effect in a moiré heterostructure. *Science* **367**, 900–903 (2020).
27. Li, T. et al. Quantum anomalous Hall effect from intertwined moiré bands. *Nature* **600**, 641–646 (2021).
28. Wu, F., Lovorn, T., Tutuc, E., Martin, I. & Macdonald, A. H. Topological insulators in twisted transition metal dichalcogenide homobilayers. *Phys. Rev. Lett.* **122**, 086402 (2019).
29. Li, H., Kumar, U., Sun, K. & Lin, S. Z. Spontaneous fractional Chern insulators in transition metal dichalcogenide moiré superlattices. *Phys. Rev. Res.* **3**, L032070 (2021).
30. Devakul, T., Crépel, V., Zhang, Y. & Fu, L. Magic in twisted transition metal dichalcogenide bilayers. *Nat. Commun.* **12**, 6730 (2021).
31. Yu, H., Chen, M. & Yao, W. Giant magnetic field from moiré induced Berry phase in homobilayer semiconductors. *Natl Sci. Rev.* **7**, 12–20 (2020).
32. Crépel, V. & Fu, L. Anomalous Hall metal and fractional Chern insulator in twisted transition metal dichalcogenides. *Phys. Rev. B* **107**, L201109 (2023).
33. Ledwith, P. J., Tarnopolsky, G., Khalaf, E. & Vishwanath, A. Fractional Chern insulator states in twisted bilayer graphene: an analytical approach. *Phys Rev Res* **2**, 023237 (2020).
34. Abouelkomsan, A., Liu, Z. & Bergholtz, E. J. Particle-hole duality, emergent fermi liquids, and fractional Chern insulators in moiré flatbands. *Phys. Rev. Lett.* **124**, 106803 (2020).
35. Devakul, T. et al. Magic-angle helical trilayer graphene. *Sci. Adv.* **9**, eadi6063 (2023).
36. Zhang, Y. H., Mao, D., Cao, Y., Jarillo-Herrero, P. & Senthil, T. Nearly flat Chern bands in moiré superlattices. *Phys. Rev. B* **99**, 075127 (2019).
37. Gao, Q., Dong, J., Ledwith, P., Parker, D. & Khalaf, E. Untwisting moiré physics: almost ideal bands and fractional Chern insulators in periodically strained monolayer graphene. *Phys. Rev. Lett.* **131**, 096401 (2023).
38. Repellin, C. & Senthil, T. Chern bands of twisted bilayer graphene: fractional Chern insulators and spin phase transition. *Phys. Rev. Res.* **2**, 023238 (2020).
39. Spanton, E. M. et al. Observation of fractional Chern insulators in a van der Waals heterostructure. *Science* **360**, 62–66 (2018).
40. Xie, Y. et al. Fractional Chern insulators in magic-angle twisted bilayer graphene. *Nature* **600**, 439–443 (2021).
41. Koshino, M. & McCann, E. Trigonal warping and Berry's phase Nπ in ABC-stacked multilayer graphene. *Phys. Rev. B* **80**, 165409 (2009).

42. Zhang, F., Jung, J., Fiete, G. A., Niu, Q. & MacDonald, A. H. Spontaneous quantum Hall states in chirally stacked few-layer graphene systems. *Phys. Rev. Lett.* **106**, 156801 (2011).
43. Park, Y., Kim, Y., Chittari, B. L. & Jung, J. Topological flat bands in rhombohedral tetralayer and multilayer graphene on hexagonal boron nitride moire superlattices. *Phys. Rev. B.* **108**, 155406 (2023).
44. Regan, E. C. et al. Mott and generalized Wigner crystal states in WSe_2/WS_2 moiré superlattices. *Nature* **579**, 359–363 (2020).
45. Xu, Y. et al. Correlated insulating states at fractional fillings of moiré superlattices. *Nature* **587**, 214–218 (2020).
46. Smoleński, T. et al. Signatures of Wigner crystal of electrons in a monolayer semiconductor. *Nature* **595**, 53–57 (2021).
47. Goldman, H., Reddy, A. P., Paul, N. & Fu, L. Zero-field composite Fermi liquid in twisted semiconductor bilayers. *Phys. Rev. Lett.* **131**, 136501 (2023).
48. Dong, J., Wang, J., Ledwith, P. J., Vishwanath, A. & Parker, D. E. Composite Fermi liquid at zero magnetic field in twisted $MoTe_2$. *Phys. Rev. Lett.* **131**, 136502 (2023).
49. Barkeshli, M. & McGreevy, J. Continuous transitions between composite Fermi liquid and Landau Fermi liquid: a route to fractionalized Mott insulators. *Phys. Rev. B. Condens. Matter Mater. Phys.* **86**, 075136 (2012).
50. Song, X.-Y., Zhang, Y.-H. & Senthil, T. Phase transitions out of quantum Hall states in moire TMD bilayers. Preprint at https://arxiv.org/abs/2308.10903 (2023).

Methods

Device fabrication

The pentalayer graphene and hBN flakes were prepared by mechanical exfoliation onto SiO_2–Si substrates. The rhombohedral domains of pentalayer graphene were identified using near-field infrared microscopy[51], confirmed with Raman spectroscopy and isolated by cutting with a Bruker atomic force microscope[52]. The van der Waals heterostructure was made following a dry transfer procedure. We picked up the top hBN, graphite, middle hBN and the pentalayer graphene using polypropylene carbonate film and landed it on a prepared bottom stack consisting of an hBN and graphite bottom gate. The device was then etched into a Hall bar structure using standard e-beam lithography and reactive-ion etching. We deposited Cr–Au for electrical connections to the source, drain and gate electrodes.

Previous experimental works on multilayer rhombohedral graphene

Multilayer rhombohedral graphene with a layer number greater than two has been studied heavily in the experiment. In highly tuneable electronic bands in crystalline multilayer rhombohedral graphene[53–56], correlated insulators, superconductivity, Chern insulators, orbital magnetism and multiferroicity have been demonstrated[53,56–63]. When placed on hBN to form a moiré superlattice, rhombohedral graphene shows Mott insulators, tuneable ferromagnetism and Chern insulators, as well as superconductivity[64–67].

Previous experiments adopted three different device configurations: (1) rhombohedral graphene on a SiO_2 substrate[53–55]; (2) suspended rhombohedral graphene[56,57] and (3) rhombohedral graphene encapsulated by hBN[58–67]. Our devices are in the third category, which balance high device quality, large parameter space enabled by high gate voltages and several terminals that allow the decoupling of R_{xx} and R_{xy}. These factors all contribute to the experimental observation of FQAHE.

Transport measurement

The device was measured in a Bluefors LD250 dilution refrigerator with an electronic temperature of around 100 mK. Stanford Research Systems SR830 lock-in amplifiers were used to measure the longitudinal and Hall resistance R_{xx} and R_{xy} with an a.c. frequency at 17.77 Hz. For constant voltage measurement, a voltage bias of 60 μV was applied. For constant current measurement, a current bias of 2 nA was applied. Keithley 2400 source meters were used to apply top and bottom gate voltages. Top-gate voltage V_t and bottom gate voltage V_b were swept to adjust doping density $n_e = (C_tV_t + C_bV_b)/e$ and displacement field $D/\varepsilon_0 = (C_tV_t - C_bV_b)/2$, where C_t and C_b are the top-gate and bottom gate capacitance per area, respectively, calculated from the Landau fan diagram.

Disentangling longitudinal and Hall resistance

The optical images of the two devices are shown in Extended Data Fig. 1c,d. Two contacts on one side of the device did not work and were floated during the measurement. The device geometry was such that no pair of contacts allowed a perfect measurement of pure R_{xy} or R_{xx}. To disentangle R_{xx} and R_{xy} in the resistance tensor, we used the magnetic field symmetrization and antisymmetrization method[26,59,68]. The longitudinal resistance and Hall resistance can be separated by using the magnetic field symmetrization and antisymmetrization method on the basis that R_{xx} is symmetric with B, whereas R_{xy} is antisymmetric. Measurements performed at opposite magnetic fields (larger than the coercive field) can thus be used to extract R_{xx} and R_{xy} at $B = 0$ for the QAH states, as follows:

$$R_{xx}(0) = (R(B) + R(-B))/2 \quad R_{xy}(0) = (R(B) - R(-B))/2$$

In Extended Data Fig. 4. we demonstrate the field symmetrization and antisymmetrization method step by step from the raw data to the plot we used in Fig. 1b,c as an example. For simplicity, $R_{12,34}$ corresponds to a resistance measured by applying current from contact number 1 to 2 and measuring the voltage between nos. 3 and 4. $R_{13,24}$ is measured at $B = \pm 100$ mT as shown in Extended Data Fig. 4a,b. The R_{xy} can be obtained by extracting the field antisymmetric part of $R_{13,24}$ or $R_{24,13}$, as follows:

$$R_{xy}(0) = (R_{13,24}(100\,\mathrm{mT}) - R_{13,24}(-100\,\mathrm{mT}))/2$$

As the longitudinal component is symmetric with respect to the magnetic field, it will be cancelled by this subtraction process at the same magnitude of magnetic field but with the opposite sign. Therefore, the disentangled R_{xy} could be obtained, which is plotted in Extended Data Fig. 4c and used in Fig. 1c. Following the same argument, resistance measurement of $R_{23,14}$ is performed at $B = \pm 100$ mT as shown in Extended Data Fig. 4d,e. The longitudinal resistance can be separated by:

$$R_{xx}(0) = (R_{23,14}(100\,\mathrm{mT}) + R_{23,14}(-100\,\mathrm{mT}))/2$$

As the Hall resistance is antisymmetric with respect to the magnetic field, it will be perfectly removed by this summation process at the opposite magnetic field. So that longitudinal resistance can be separated and plotted in Extended Data Fig. 4f, it is also shown in Fig. 1b.

In Figs. 1c and 2c we plotted $(R_{xy}(0.1\,\mathrm{T}) - R_{xy}(-0.1\,\mathrm{T}))/2$, whereas in Figs. 2e,f, 3b,c and 4a,c we plotted $(R_{xy}(-0.1\,\mathrm{T}) - R_{xy}(0.1\,\mathrm{T}))/2$ for the convenience of presentation.

Apart from disentangling longitudinal and Hall resistance, measurement at a magnetic field larger than the coercive field also eliminates the random fluctuations of the magnetic domains at zero magnetic field, which is typical for micro-sized devices. As shown in Extended Data Fig. 6a, spikes appear randomly in all curves at $B = 0$ as we scan the moiré filling factor υ. These fluctuations correspond to the random switching of the orbital magnetization in our micrometre-sized devices. At $B = \pm 100$ mT, these fluctuations are completely suppressed. We have also performed scans at even smaller magnetic fields. As shown in Extended Data Fig. 6b, all the curves at $B = 10$, 50 and 100 mT overlap well. Therefore, we used the magnetic field of ±0.1 T just to avoid fluctuations, whereas the phenomena we observed is robust at $B = 0$.

Magnetic hysteresis measurements of R_{xx} and R_{xy}

The four-probe magnetic hysteresis measurements with all possible pin combinations and the results of raw data and data after processing at $\upsilon = 3/5$ in Extended Data Fig. 5 as an example. First, we used the magnetic field symmetrization and antisymmetrization method to disentangle R_{xx} and R_{xy}. Magnetic field sweep of $R_{13,24}$ is shown as solid (dashed) line in Extended Data Fig. 5a. In this case, Hall resistance can be extracted by following the field antisymmetrization method:

$$R_{xy\_solid} = (R_{13,24\_solid}(+B) - R_{13,24\_dash}(-B))/2.$$
$$R_{xy\_dash} = (R_{13,24\_dash}(+B) - R_{13,24\_solid}(-B))/2$$

The obtained R_{xy} is plotted in Extended Data Fig. 5g with anomalous Hall value equal to the quantized value at $\upsilon = 3/5$. On the basis of the raw data shown in Extended Data Fig. 5b, magnetic field sweep of $R_{24,13}$ can be treated in a similar way:

$$R_{xy\_solid} = (R_{24,13\_solid}(+B) - R_{24,13\_dash}(-B))/2.$$
$$R_{xy\_dash} = (R_{24,13\_dash}(+B) - R_{24,13\_solid}(-B))/2$$

The hysteresis loop after antisymmetrization is shown in Extended Data Fig. 5h.

The magnetic sweep of longitudinal resistance can be extracted on the basis of the raw data from $R_{14,23}$ and $R_{23,14}$ measurements by following the magnetic field symmetrization method:

$$R_{xx\_solid} = (R_{14,23\_solid}(+B) + R_{14,23\_dash}(-B))/2.$$
$$R_{xx\_dash} = (R_{14,23\_dash}(-B) + R_{14,23\_solid}(+B))/2$$

$$R_{xx\_solid} = (R_{23,14\_solid}(+B) + R_{23,14\_dash}(-B))/2.$$
$$R_{xx\_dash} = (R_{23,14\_dash}(-B) + R_{23,14\_solid}(+B))/2$$

The symmetrized R_{xx} is plotted in Extended Data Fig. 5i,l.

Other than relying on the symmetrization and antisymmetrization with respect to the magnetic field, we also performed symmetrization and antisymmetrization by using the Onsager reciprocal relation to better capture the behaviours of the magnetic domain[26,59,68]. $R_{14,23}$ and its Onsager reciprocal $R_{23,14}$ are mainly contributed to by R_{xx}. The symmetrization can then be performed by following:

$$R_{xx\_solid} = (R_{14,23\_solid} + R_{23,14\_solid})/2.$$
$$R_{xx\_dash} = (R_{14,23\_dash} + R_{23,14\_dash})/2$$

The hysteresis loop of the disentangled longitudinal resistance obtained by the Onsager reciprocal relation is plotted in Extended Data Fig. 5n. Similarly, $R_{24,13}$ and its Onsager reciprocal $R_{13,24}$ are dominated by R_{xy}. The longitudinal part can be eliminated by performing the following antisymmetrization process:

$$R_{xy\_solid} = (R_{13,24\_solid} - R_{24,13\_solid})/2.$$
$$R_{xy\_dash} = (R_{24,13\_dash} - R_{13,24\_dash})/2$$

As we can see from Extended Data Fig. 5c,f,m, no matter what symmetrization method we use, the Hall resistance value always stay quantized at $B = 0$. As the physics we address in the paper is not about magnetic domain, symmetrization and antisymmetrization with respect to the magnetic field are used for the hysteresis loops in Figs. 2a,b, 3d–j and 4b,d.

Phenomenological model for moiré bands

We calculate the band structure shown in Fig. 1d starting from the $k{\cdot}p$ Hamiltonian of ref. 43 for (moiré-less) n-layer rhombohedral graphene with $n = 5$ and $t_0 = -2.6$ eV for nearest-neighbour intralayer hopping. Using the hBN moiré potential model from ref. 43, which only couples directly to the adjacent graphene layer, we do not obtain an isolated $|C| = 1$ band at a large displacement field. We note, however, that the nearly aligned hBN layer will induce a charge density modulation and the resulting Hartree–Fock potential will act on all layers. This motivates us to consider the following phenomenological model:

$$H = H_0(\mathbf{k}) + V(\mathbf{r})$$

where $H_0(\mathbf{k})$ is the moiré-less $k{\cdot}p$ Hamiltonian and

$$V(\mathbf{r}) = -2V_0 \sum_{i=1,3,5} \cos(\mathbf{g}_i \cdot \mathbf{r} + \phi)$$

is a superlattice potential that acts identically on all layers. We choose $V_0 = 10$ meV, $\phi = 0$. We note that the appearance of an isolated $|C| = 1$ band does not rely on fine tuning of these parameters or the potential acting equally on all layers. Here the moiré reciprocal lattice vectors are $\mathbf{g}_1 = (\epsilon - \theta\hat{z}\times)\left(0, \frac{4\pi}{a_0\sqrt{3}}\right)$ where $\epsilon = 0.017$ is the graphene–hBN lattice constant mismatch and we choose $\theta = 0.744\pi/180$ to achieve a moiré period $a_M = \frac{4\pi}{\sqrt{3}\,|\mathbf{g}_1|} = 11.5$ nm as determined experimentally.

Data availability

The data shown in the main figures are available from https://doi.org/10.7910/DVN/T4QPNP. Other data that support the findings of this study are available from the corresponding authors upon reasonable request.

51. Ju, L. et al. Topological valley transport at bilayer graphene domain walls. *Nature* **520**, 650–655 (2015).
52. Li, H. et al. Electrode-free anodic oxidation nanolithography of low-dimensional materials. *Nano Lett.* **18**, 8011–8015 (2018).
53. Bao, W. et al. Stacking-dependent band gap and quantum transport in trilayer graphene. *Nat. Phys.* **7**, 948–952 (2011).
54. Zhang, L., Zhang, Y., Camacho, J., Khodas, M. & Zaliznyak, I. The experimental observation of quantum Hall effect of $l = 3$ chiral quasiparticles in trilayer graphene. *Nat. Phys.* **7**, 953–957 (2011).
55. Zou, K., Zhang, F., Clapp, C., MacDonald, A. H. & Zhu, J. Transport studies of dual-gated ABC and ABA trilayer graphene: band gap opening and band structure tuning in very large perpendicular electric fields. *Nano Lett.* **13**, 369–373 (2013).
56. Lee, Y. et al. Competition between spontaneous symmetry breaking and single-particle gaps in trilayer graphene. *Nat. Commun.* **5**, 5656 (2014).
57. Myhro, K. et al. Large tunable intrinsic gap in rhombohedral-stacked tetralayer graphene at half filling. *2D Mater.* **5**, 045013 (2018).
58. Shi, Y. et al. Electronic phase separation in multilayer rhombohedral graphite. *Nature* **584**, 210–214 (2020).
59. Zhou, H. et al. Half- and quarter-metals in rhombohedral trilayer graphene. *Nature* **598**, 429–433 (2021).
60. Zhou, H., Xie, T., Taniguchi, T., Watanabe, K. & Young, A. F. Superconductivity in rhombohedral trilayer graphene. *Nature* **598**, 434–438 (2021).
61. Han, T. et al. Correlated insulator and Chern insulators in pentalayer rhombohedral stacked graphene. *Nat. Nanotechnol.* https://doi.org/10.1038/s41565-023-01520-1 (2023).
62. Han, T. et al. Orbital multiferroicity in pentalayer rhombohedral graphene. *Nature* **623**, 41–47 (2023).
63. Liu, K. et al. Interaction-driven spontaneous broken-symmetry insulator and metals in ABCA tetralayer graphene. *Nat. Nanotechnol.* https://doi.org/10.1038/s41565-023-01558-1 (2023).
64. Chen, G. et al. Evidence of a gate-tunable Mott insulator in a trilayer graphene moiré superlattice. *Nat. Phys.* **15**, 237–241 (2019).
65. Chen, G. et al. Tunable orbital ferromagnetism at noninteger filling of a moiré superlattice. *Nano Lett.* **22**, 238–245 (2022).
66. Chen, G. et al. Tunable correlated Chern insulator and ferromagnetism in a moiré superlattice. *Nature* **579**, 56–61 (2020).
67. Chen, G. et al. Signatures of tunable superconductivity in a trilayer graphene moiré superlattice. *Nature* **572**, 215–219 (2019).
68. Sample, H. H., Bruno, W. J., Sample, S. B. & Sichel, E. K. Reverse-field reciprocity for conducting specimens in magnetic fields. *J. Appl. Phys.* **61**, 1079–1084 (1987).

Acknowledgements We acknowledge helpful discussions with X.G. Wen, T. Senthil, P. Lee, F. Wang and R. Ashoori. We thank D. Laroche for assistance with early investigation of a related sample. L.J. acknowledges support from a Sloan Fellowship. Work by T.H., J.Y. and J.S. was supported by NSF grant no. DMR-2225925. The device fabrication of this work was supported by the STC Center for Integrated Quantum Materials, NSF grant no. DMR-1231319 and was carried out at the Harvard Center for Nanoscale Systems and MIT.Nano. Part of the device fabrication was supported by USD(R&E) under contract no. FA8702-15-D-0001. K.W. and T.T. acknowledge support from the JSPS KAKENHI (grant nos. 20H00354, 21H05233 and 23H02052) and World Premier International Research Center Initiative (WPI), MEXT, Japan. A.P.R. was supported by the Air Force Office of Scientific Research (AFOSR) under award no. FA9550-22-1-0432. L.F. was supported by the STC Center for Integrated Quantum Materials (CIQM) under NSF award no. DMR-1231319.

Author contributions L.J. supervised the project. Z.L. and T.H. performed the d.c. magneto-transport measurement. T.H. and Y.Y. fabricated the devices. J.Y., J.S., Z.L. and T.H. helped with installing and testing the dilution refrigerator. A.P.R. and L.F. performed the calculations. K.W. and T.T. grew hBN crystals. All authors discussed the results and wrote the paper.

Competing interests The authors declare no competing interests.

Additional information

Supplementary information The online version contains supplementary material available at https://doi.org/10.1038/s41586-023-07010-7.

Correspondence and requests for materials should be addressed to Long Ju.

Peer review information *Nature* thanks Anindya Das and the other, anonymous, reviewer(s) for their contribution to the peer review of this work. Peer reviewer reports are available.

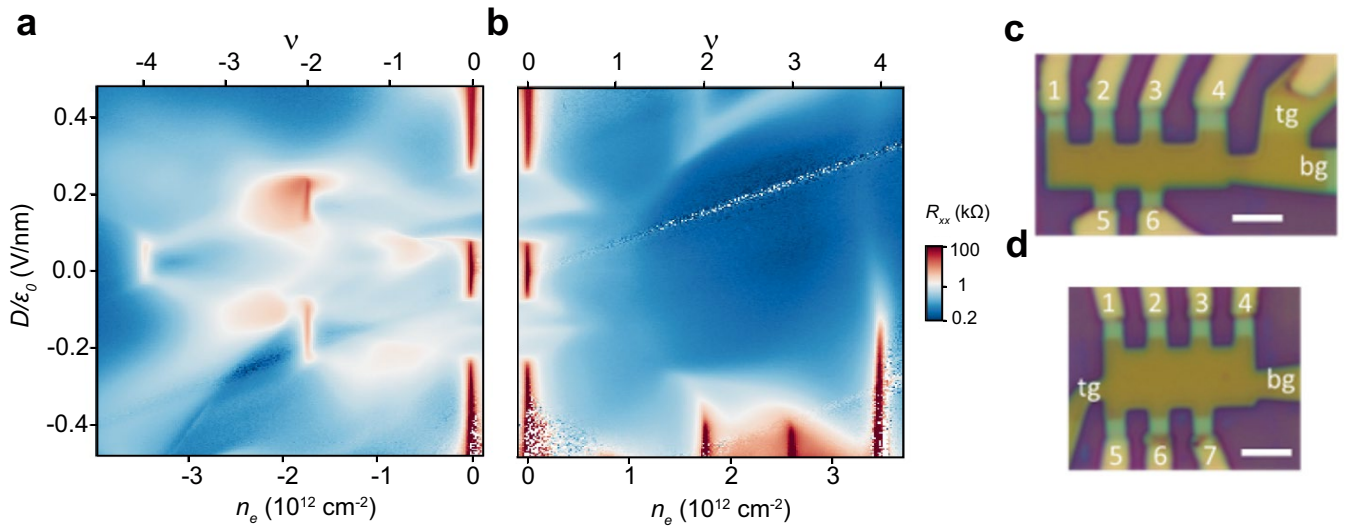

Extended Data Fig. 1 | Phase diagram and optical micrographs of our devices. a&**b** corresponds to the hole-doping and electron-doping sides, respectively. The hole side shows resistive states at filling factors $\nu = -2$ and -4, while the electron side shows correlated insulating states at $\nu = 2, 3$ and 4 at $D < 0$—opposite side of D at which we observed IQAHE and FQAHEs. **c**. Device 1 from which the data in the main text is taken. Scale bar: 3 μm **d**. Device 2, the data of which is included in Extended Data Fig. 8 & 9. Scale bar:3 μm.

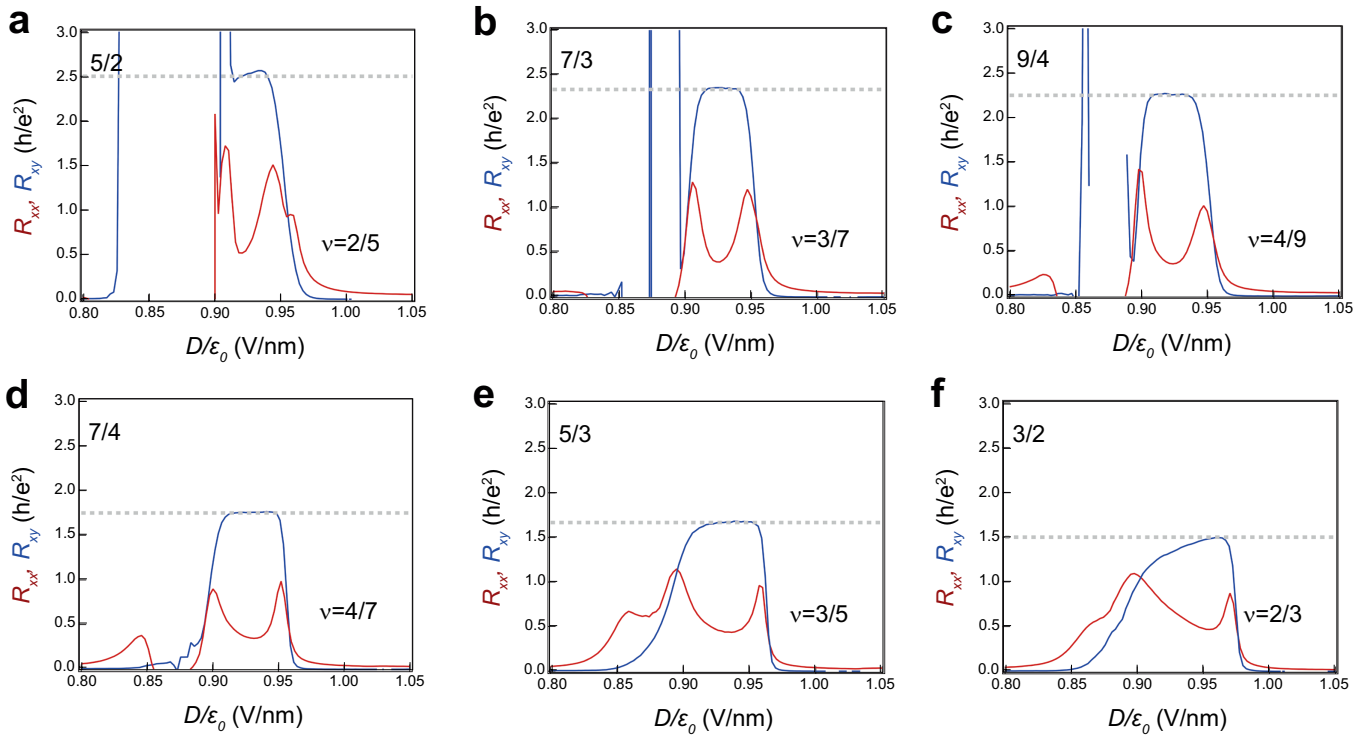

Extended Data Fig. 2 | Gate displacement field dependence of R_{xx} and R_{xy} at fractional filling factors for Device 1. Each FQAH state shows quantized R_{xy} in a range of D, while the center of this range for different states shifts with the filling factor. The D corresponding to the minimum of R_{xx} also shifts with the filling factor in the same direction.

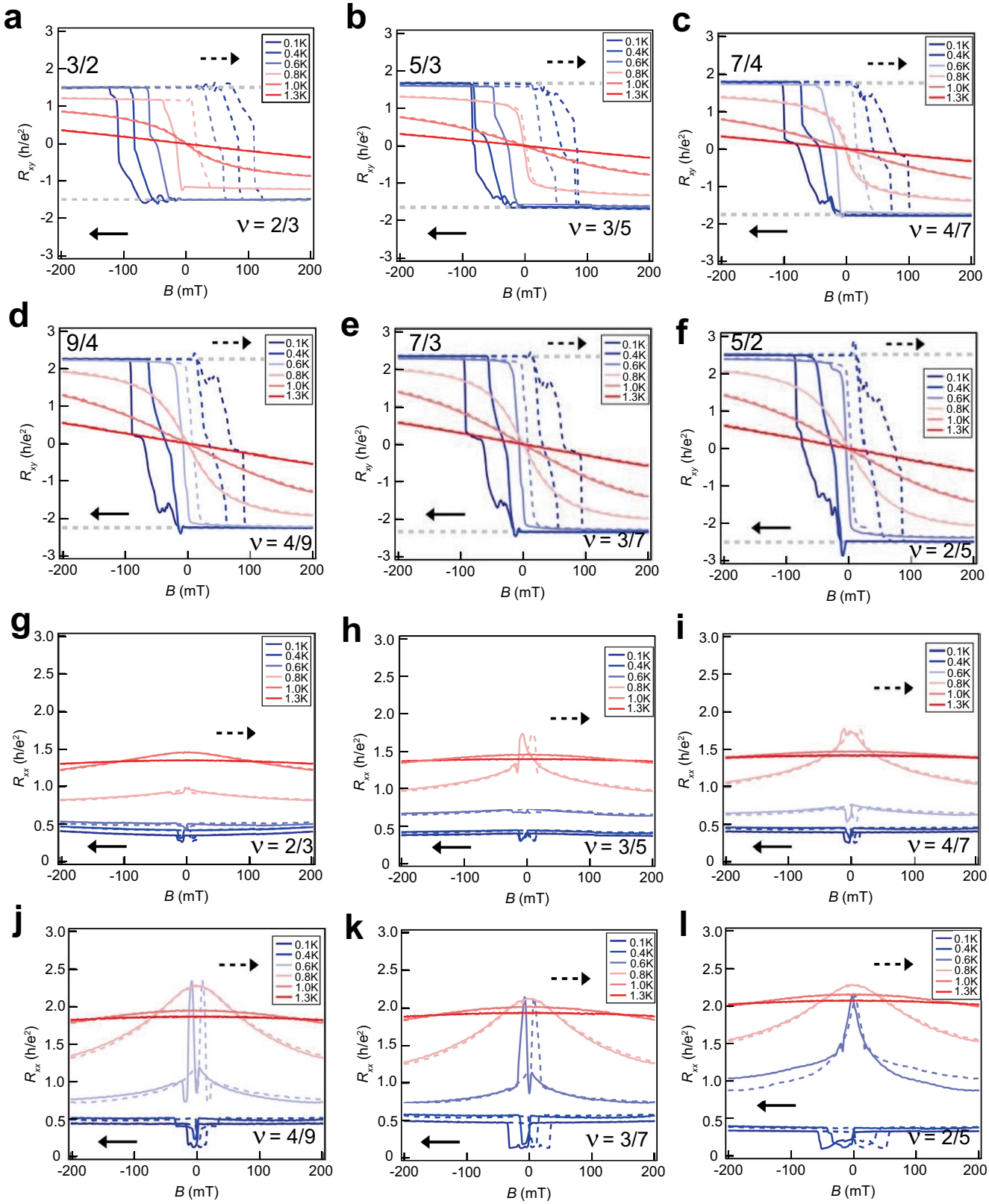

Extended Data Fig. 3 | Temperature dependence of FQAH states. a–f. Temperature dependence of R_{xy}. All states still remain quantized at 400 mK. **g–l.** Temperature dependence of R_{xx}.

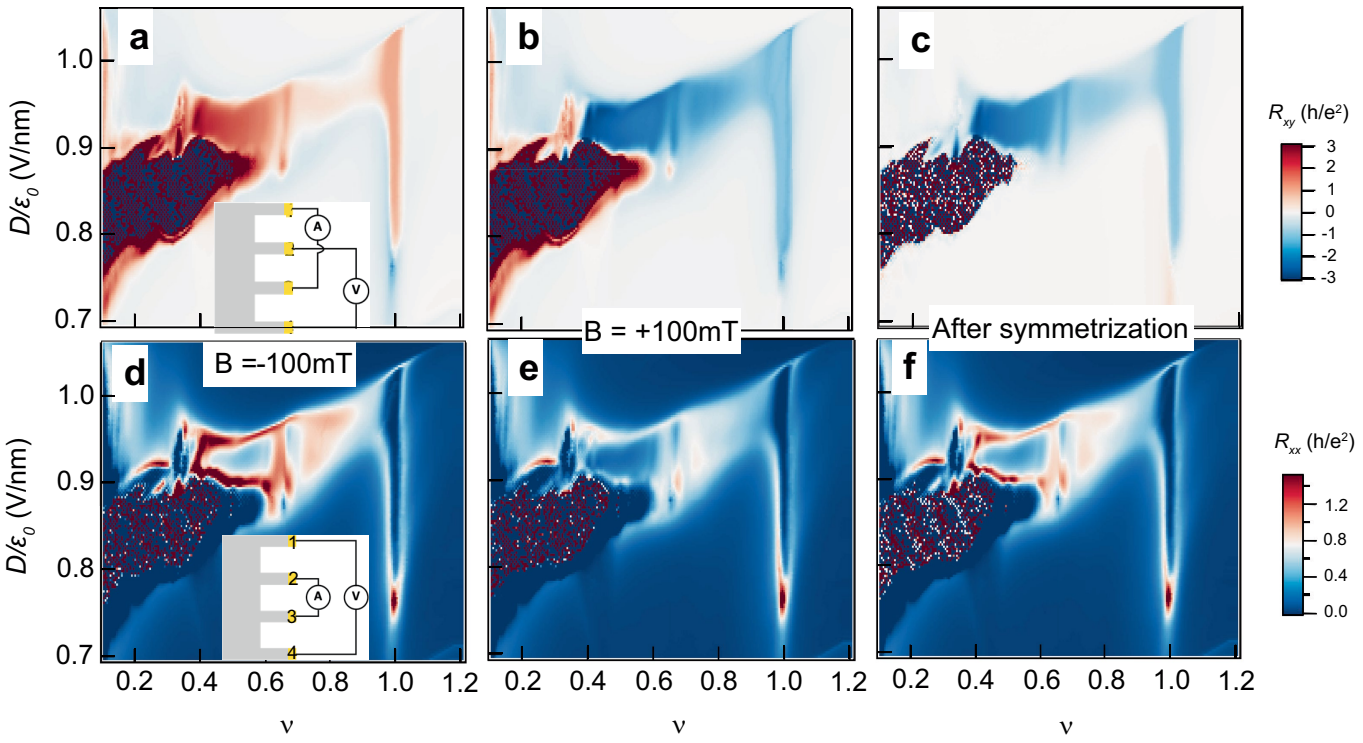

Extended Data Fig. 4 | Symmetrization/anti-symmetrization method to obtain Fig. 1b & c. **a**,**b** & **d**,**e**. Raw data of $R_{13,24}$ and $R_{23,14}$ measured as functions of displacement field and moiré filling factor ν at $B = \pm 100$ mT. The insets show the measurement pin configurations. **c**&**f**. R_{xy} and R_{xx} obtained after the symmetrization/anti-symmetrization process.

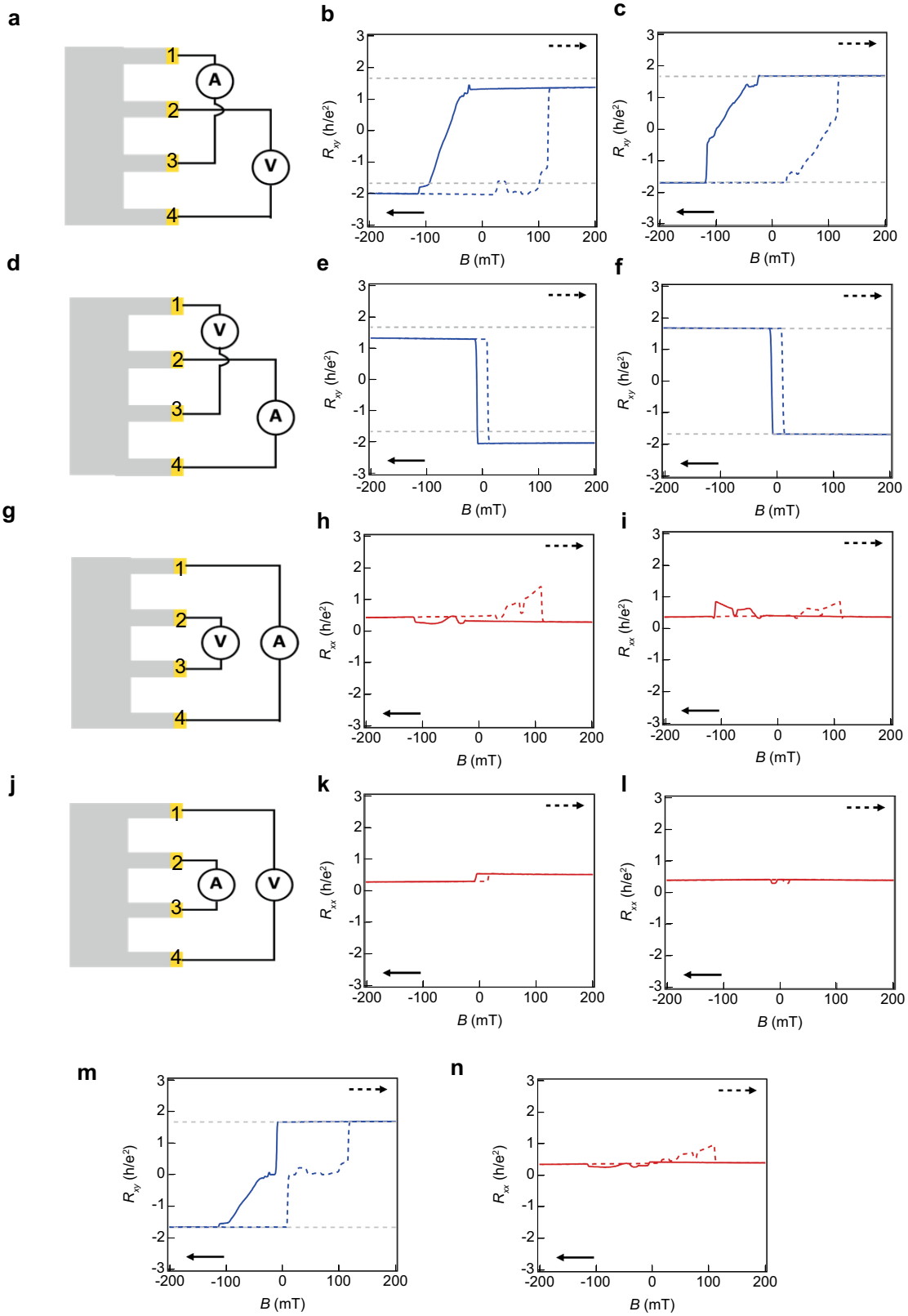

Extended Data Fig. 5 | Symmetrization/anti-symmetrization method to obtain magnetic hysteresis data at $\nu = 3/5$. a, **b**, **d**, **e**, **g**, **h**, **j** & **k**. Raw data of $R_{13,24}$, $R_{24,13}$, $R_{14,23}$ and $R_{23,14}$ measured as functions of magnetic field. The insets show the measurement pin configurations. **c**, **f**, **i**&**l**. R_{xy} and R_{xx} obtained after the symmetrization process. **m**&**n**. R_{xy} and R_{xx} extracted after the symmetrization/anti-symmetrization process using the Onsager reciprocal relation.

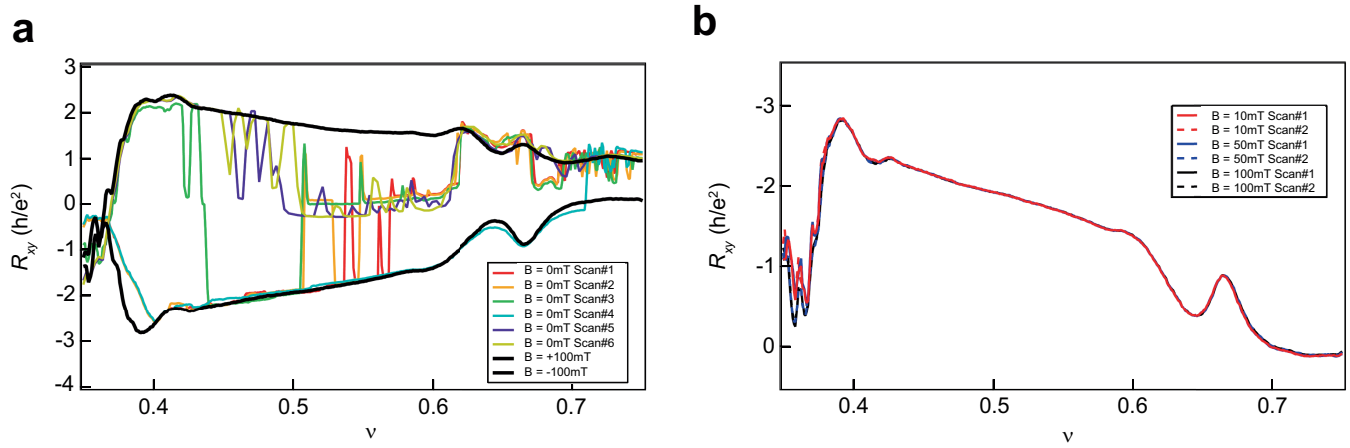

Extended Data Fig. 6 | R_{xy} line scans at small magnetic fields. a. R_{xy} line scan versus moiré filling factor υ at $D/\varepsilon O$ = 0.9 V/nm. Curves with rainbow colors represent multiple scans at B = 0. Black curves show scans at B = ± 100 mT. **B.** R_{xy} line scans versus υ at B = 10 mT, 50 mT, 100 mT.

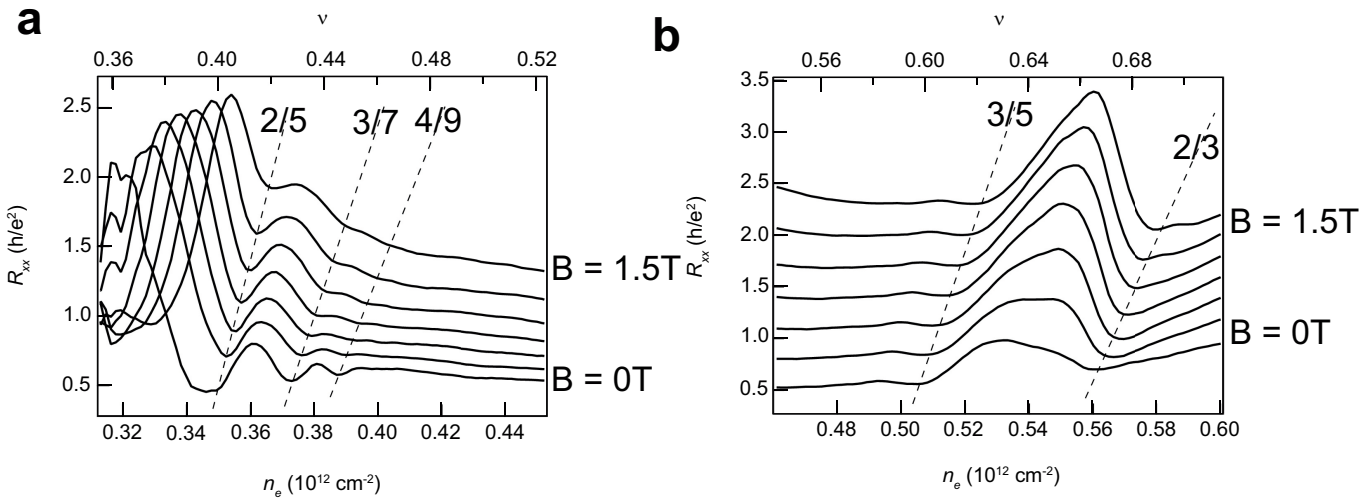

Extended Data Fig. 7 | R_{xx} line scans at varying magnetic field. a & **b**. R_{xx} line scans with moiré filling factor $\nu < 1/2$ and $\nu > 1/2$, respectively. Dips at fractional filling factors shift with magnetic field as indicated by the dashed lines. Curves are equally shifted vertically for clarity.

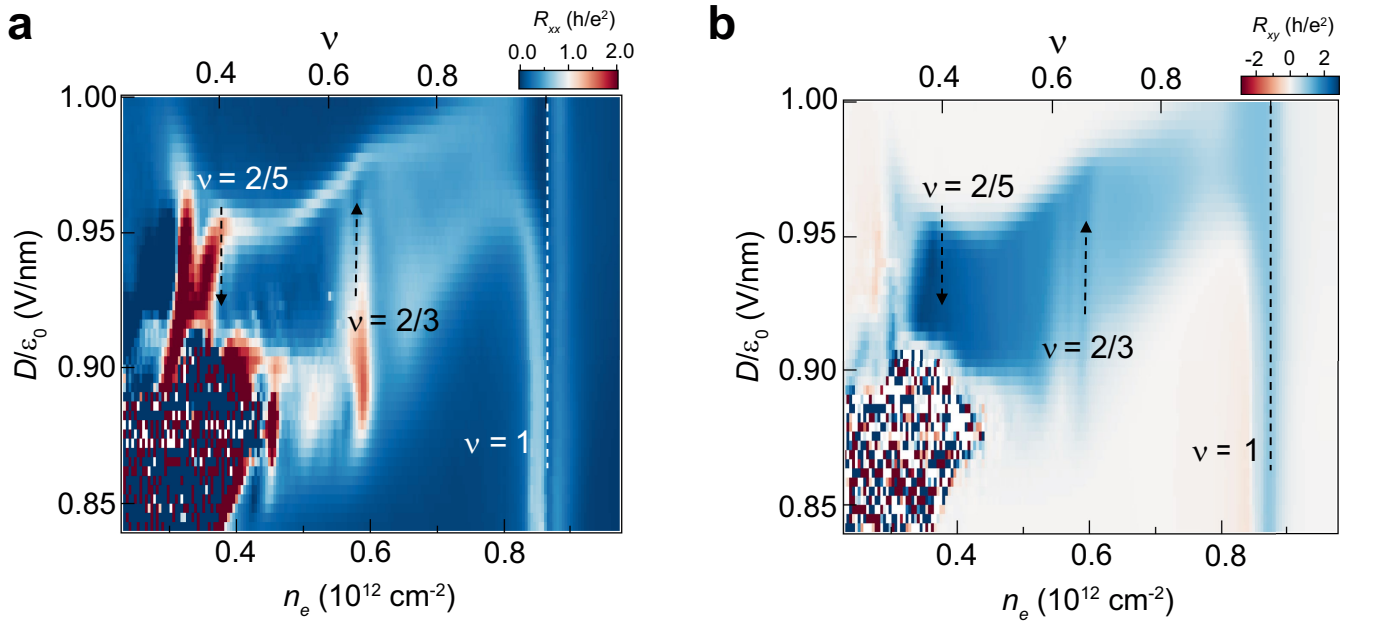

Extended Data Fig. 8 | Data from Device 2. a & **b**. Phase diagrams of the device revealed by symmetrized R_{xx} and anti-symmetrized R_{xy} at $B = \pm 0.1$ T as functions of charge density n_e (filling factor ν) and D. The temperature at the mixing chamber of dilution refrigerator is 10 mK. Clear dips of R_{xx} can be seen at filling factors of the moiré superlattice $\nu = 1, 2/3$ and $2/5$ (indicated by the dashed lines and arrows), where R_{xy} shows plateaus of values.

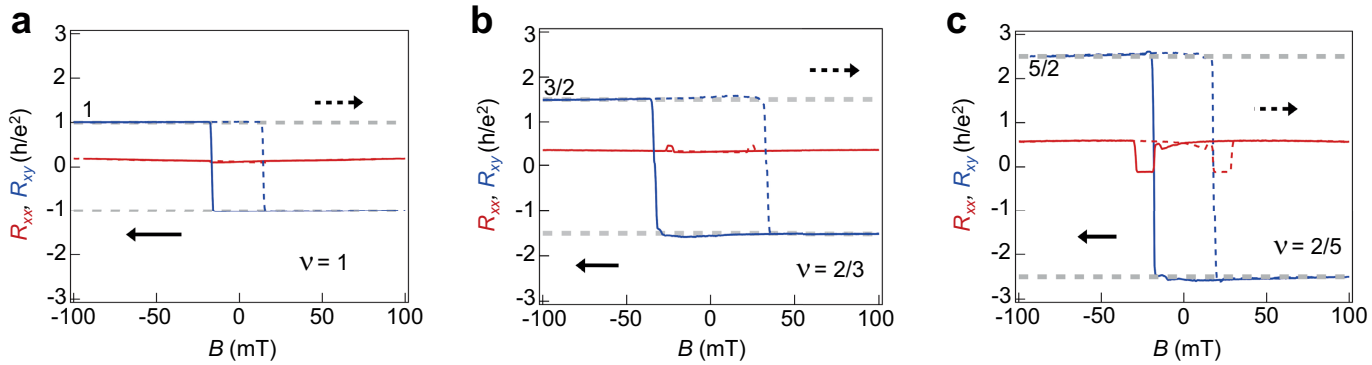

Extended Data Fig. 9 | Magnetic hysteresis data from Device 2. a–**c**. Magnetic hysteresis measurements at $\nu = 1, 2/3$ and $2/5$. Clear hysteresis and values of R_{xy} at $\frac{h}{\nu e^2}$ can been seen.